Journal of Metals, Materials and Minerals, 36(4), e2538, 2026

Non-destructive silicon quantification in low-level Si-doped diamond-like carbon films

Nanthapat CHANAPAI[1], and Phitsanu POOLCHARUANSIN[1,*]

[1] *Department of Physics, Faculty of Science, Mahasarakham University, Mahasarakham, 44150, Thailand*

***Corresponding author e-mail**: phitsanu.p@msu.ac.th

Received date:
23 October 2025
Revised date:
9 July 2026
Accepted date:
21 July 2026

Keywords:
Diamond-like carbon;
Silicon doping;
Co-deposition;
Raman spectroscopy;
X-ray photoelectron spectroscopy

Abstract

Diamond-like carbon (DLC) films offer exceptional mechanical and chemical properties but face limitations in adhesion and thermal stability, which restrict their broader applications. Current characterization methods for silicon-doped DLC films rely on destructive techniques, which pose challenges for industrial quality control. We investigate the effects of low-level silicon doping on the microstructure and optical properties of DLC while developing a non-destructive quantification method. Films were synthesized by co-deposition combining pulsed filtered cathodic vacuum arc and RF magnetron sputtering. Silicon incorporation was controlled by varying RF power up to 30 W. Characterization employed X-ray photoelectron spectroscopy (XPS), Raman spectroscopy, and spectroscopic ellipsometry, yielding silicon concentrations of 1.55 at.% to 4.64 at.% as determined by XPS. Microstructural analysis reveals C–Si bond formation and strengthened tetrahedral bonding networks with reduced graphitic clusters upon silicon doping. Wavelength-averaged optical properties show systematic decreases in both extinction coefficient and refractive index with increasing silicon content. Spectroscopic ellipsometry combined with Bruggeman effective-medium approximation modeling achieved a strong linear correlation ($R^2 = 0.97$) with XPS-measured silicon concentrations. This non-destructive quantification at sub-5 at.% silicon levels, beyond the sensitivity range of conventional destructive techniques, offers a practical route to industrial-scale quality control of Si–DLC films.

1. Introduction

Diamond-like carbon (DLC) films have attracted significant attention from industrial and academic sectors due to their exceptional combination of properties derived from their unique amorphous structure. These films comprise carbon atoms in both sp^2 (graphite-like) and sp^3 (diamond-like) hybridizations, where sp^2 configurations primarily contribute to electrical conductivity and lubrication properties, while sp^3 bonding governs hardness and chemical inertness. This dual bonding enables DLC films to exhibit high hardness, low friction coefficients, excellent wear resistance, and superior chemical stability. These properties are suitable for protective coatings on tools, molds, and automotive components [1–3].

Despite these advantageous properties, DLC films face significant limitations that restrict their broader application. Poor adhesion to metal substrates is a primary challenge, often due to high internal compressive stress generated during deposition. This stress can cause film delamination under external forces, particularly as film thickness increases [4]. Strategies such as interlayer coatings or multilayer structures have been employed to improve adhesion and reduce internal stress [5,6]. Another critical limitation is the structural instability of DLC films at elevated temperatures, where sp^3 bonds may transform to sp^2 configurations, leading to oxidation, reduced corrosion resistance, and reduced hardness [7].

To address these challenges, doping DLC films with various elements has been explored, including oxygen, nitrogen, fluorine, transition metals, and silicon [8,9], with related microstructural and process-control studies of carbon-based thin films further supporting the role of deposition parameters in tailoring film composition [10,11]. Silicon-doped DLC (Si–DLC) has gained particular interest due to enhanced mechanical, electrical, and chemical properties that expand application possibilities. For example, silicon incorporation improves tribological characteristics by reducing friction coefficients and residual stress [8]. In addition, several studies have demonstrated the effectiveness of silicon doping for improving thermal stability [12–14] and corrosion resistance [15,16]. The formation of Si–C bonds contributes to thermal stability and friction reduction [12,17], while silicon incorporation significantly reduces internal stress of the films [18,19].

Understanding and controlling the microstructure and composition of Si–DLC films are essential for tailoring properties including hardness, wear resistance, and thermal stability. Spectroscopic ellipsometry (SE) is a non-destructive, contact-free technique for characterizing thin films and provides information on optical properties such as refractive index, extinction coefficient, film thickness, and surface characteristics [20–22]. The effective medium approximation (EMA) model has been applied to characterize various carbon-based materials, including evaluating density and sp^3/sp^2 ratios in DLC films [23] and quantifying dopant content in metal-doped [24] and boron-doped [25] carbon films. However, the direct application of SE combined with EMA to quantify silicon content at low doping levels (<5 at.%) in Si–DLC films remains limited in the literature.

In this work, we investigate the effects of low silicon concentrations on the microstructure of DLC films and develop a non-destructive method for estimating silicon content using spectroscopic ellipsometry

with the Bruggeman effective-medium approximation. Silicon volume fractions derived from EMA modeling are directly correlated with atomic concentrations from X-ray photoelectron spectroscopy (XPS). We establish a rapid estimation method for silicon content that could benefit industrial-scale quality control.

2. Experimental details

2.1 Thin-film preparation

The film deposition system consists of a cylindrical chamber connected to a pumping system to achieve an ultra-high vacuum. Two deposition sources were employed simultaneously. The first source utilizes RF magnetron sputtering with a 1.3-inch diameter, 99.99% pure silicon target mounted on a cathode. This cathode connects to an RF generator through a matching network to achieve impedance matching and minimize reflected power. The second source employs a pulsed cathodic arc technique with a 0.25-inch-diameter, 99.999% pure graphite rod as the cathode. A pulse forming network (PFN) drives the arc discharge with a peak current of approximately 1.28 kA, a pulse width of 1.2 ms, and a pulse frequency of about 1.3 Hz. The generated carbon plasma passes through a 90° bent magnetic filter coil that removes micron-sized particles before deposition onto the substrate.

Undoped DLC and Si–DLC films were deposited on single-sided polished p-type boron-doped (100) silicon wafers (1 inch × 1 inch). Substrates were mounted on an electrically grounded holder that could be tilted and rotated during deposition. The substrate holder was tilted 10° and rotated at 30 rpm to enable co-deposition from both sources for all deposited films, as shown in Figure 1.

Following evacuation to a base pressure below 2×10^{-7} Torr, undoped DLC films were deposited using only the pulsed cathodic arc source. Argon gas was introduced at a flow rate of 25 sccm to establish a working pressure of approximately 4×10^{-4} Torr to deposit Si–DLC films. The RF power was varied at 15, 20, and 30 W to achieve different levels of silicon incorporation. Co-deposition was performed by simultaneously operating the carbon arc source and the silicon magnetron sputtering. Ellipsometric measurements confirmed that all deposited films had thicknesses ranging from 20.7 nm to 22.7 nm (approximately 21 ± 1 nm). No intentional substrate heating or cooling was applied. The substrate remained at room temperature throughout deposition. The holder had no in-situ thermocouple, so substrate temperature was not directly monitored. Any incidental rise from plasma exposure is not expected to affect film microstructure under the conditions used.

2.2 Film characterization

Chemical composition analysis was performed using X-ray photoelectron spectroscopy (XPS) with a monochromatic Al Kα source (photon energy 1486.6 eV, 24.6 W). Prior to measurement, film surfaces were cleaned by Ar^+ ion sputtering at 1.1 nm·min^{-1} for 1 min over a 2 mm × 2 mm area to remove surface contaminants. Survey spectra were acquired in the binding energy range of 0 to 1450 eV. Atomic concentrations of carbon, silicon, and oxygen were determined from the C 1s, Si 2p, and O 1s peak areas using Shirley background subtraction and correction with atomic sensitivity factors [26].

Microstructural analysis utilized Raman spectroscopy with a 514 nm Ar^+ laser and Renishaw inVia™ InSpect confocal microscope in backscattering geometry. The laser beam was focused through a 50x objective lens onto the sample surface at ~10.5 mW. Each spectrum was collected for 30 s and averaged over two scans in the range of 1060 cm^{-1} to 2000 cm^{-1}. Raw spectra were fitted using two Gaussian peaks representing the D (disorder) and G (graphitic) bands. The area ratio I_D/I_G was used to estimate the relative content of sp^2-to sp^3-bonded carbon.

Optical properties and silicon content in Si–DLC films were analyzed using multi-wavelength ellipsometry (J.A. Woollam, M-2000XF). The Bruggeman Effective Medium Approximation (EMA) was applied to estimate silicon volume fraction in the films. Results were compared with atomic composition obtained from XPS measurements to validate the non-destructive quantification approach.

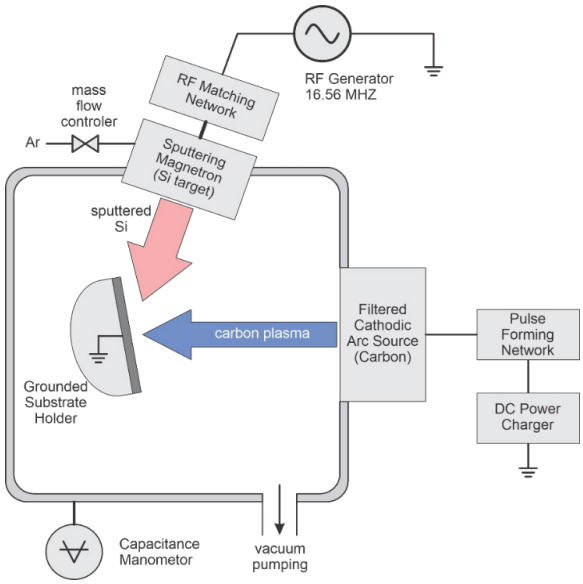

Figure 1. Schematic of the film deposition system showing the arrangement of vacuum components and deposition sources.

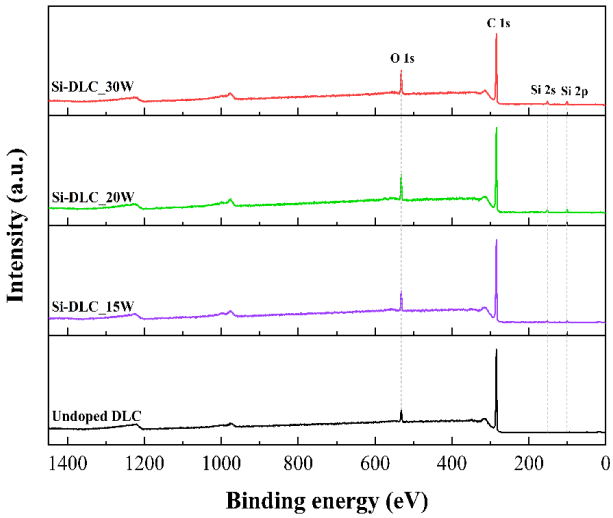

Figure 2. XPS survey spectra of undoped DLC and Si–DLC films (RF power of 0 W, 15 W, 20 W, 30 W). Labeled peaks O 1s (~532 eV), C 1s (~285 eV), Si 2s (~152 eV), and Si 2p (~101 eV). Silicon peak intensity increases with RF power.

3. Results

3.1 Compositional analysis and silicon incorporation

X-ray photoelectron spectroscopy (XPS) was employed to investigate the elemental composition and chemical bonding states of the deposited films. The survey spectrum confirmed the presence of carbon, silicon, and oxygen, with the main binding energies measured at 531.95 ± 0.01 eV for O 1s, 284.71 ± 0.05 eV for C 1s, 151.87 ± 0.02 eV for Si 2s, and 100.83 ± 0.18 eV for Si 2p, as shown in Figure 2. The peak area of each element was divided by its corresponding atomic sensitivity factor to obtain the corrected peak intensity. Atomic percentages were calculated by taking the ratio of each corrected intensity to the sum of all corrected intensities, with silicon content determined from the Si 2p peak.

Table 1 summarizes the atomic concentrations obtained from quantitative XPS analysis. The results demonstrate control over silicon incorporation through RF sputtering power adjustment. The undoped DLC film contained 92.66 at.% carbon and 7.34 at.% oxygen, with no detectable silicon. Silicon content increased progressively with RF power from 1.55 at.% at 15 W to 4.64 at.% at 30 W, reflecting the direct relationship between sputtering power and silicon incorporation efficiency. Oxygen content also increased from 7.34 at.% to 12.85 at.% with silicon doping, a phenomenon attributed to the high oxygen affinity of silicon and co-deposition dynamics discussed further below.

High-resolution XPS analysis was performed to investigate changes in chemical bonding resulting from silicon incorporation into the DLC structure. The core-level spectra of C 1s, Si 2p, and O 1s were deconvoluted to identify specific bonding components, as presented in Figure 3. The percentage of each bonding state, shown in Figure 4, was determined from the areas of the deconvoluted sub-peaks corresponding to specific chemical bonds, normalized to the total area of the corresponding core level. Table 2 provides quantitative data including precise binding energies and relative peak areas for all identified chemical bonding states, along with the calculated $sp^3/(sp^2 + sp^3)$ ratios that demonstrate the microstructural evolution with silicon content.

The Si 2p spectra exhibited two primary components namely, Si–C bonds at 100.48 ± 0.04 eV and Si–O bonds at 102.13 ± 0.15 eV (Figure 3(b)). Quantitative analysis revealed that 58.70% to 66.20% of silicon forms Si–C bonds, while 33.80% to 41.30% forms Si–O bonds (see Figure 4(b) and Table 2). The proportion of Si–C bonds decreased with increasing silicon content, from 66.20% in Si–DLC_15W to 58.70% in Si–DLC_30W. Conversely, the Si–O bond fraction increased from 33.80% to 41.30% over the same concentration range. These competitive bonding dynamics reflect the interplay between carbon network incorporation and oxygen reactivity during co-deposition. Silicon initially incorporates preferentially into the carbon network through Si–C bond formation. However, higher silicon concentrations favor increased Si–O bond formation. The increase in oxygen content with silicon doping, indicated by the rising O–Si bonding fraction, could be attributed to three sources namely (i) reaction of silicon with residual oxygen and water vapor in the chamber, given silicon's higher oxygen affinity than carbon, (ii) atmospheric exposure during sample handling and transfer, and (iii) oxygen uptake from the Ar+ pre-sputtering step prior to XPS analysis [27]. These findings align with previous studies on Si–DLC films, in which similar competitive bonding between Si–C and Si–O was observed across varying silicon concentrations [28,29].

The C 1s spectra revealed five distinct bonding environments including C–C (sp^2) at 284.08 ± 0.05 eV, C–C (sp^3) at 284.89 ± 0.04 eV, C–O at 286.24 ± 0.11 eV, C=O at 288.02 ± 0.03 eV, and C–Si at 283.68 ± 0.12 eV as shown in Figure 3(a). The emergence of the C–Si peak confirms the formation of carbon–silicon bonds within the DLC matrix. Quantitative analysis showed that the main bonding types comprised 76.92% to 78.11% C–C (sp^3), 12.90% to 18.40% C–C (sp^2), 3.78% to 8.03% C–O, 0.62% to 1.12% C=O, and an increasing proportion of C–Si bonds with higher silicon content.

Table 1. Atomic concentrations of carbon, silicon, and oxygen in undoped DLC and Si–DLC films obtained from XPS analysis.

Sample	RF power	Atomic concentration [at.%]		
	[W]	C (C 1s)	O (O 1s)	Si (Si 2p)
undoped DLC	0	92.66	7.34	—
Si–DLC_15W	15	88.06	10.39	1.55
Si–DLC_20W	20	85.03	11.64	3.32
Si–DLC_30W	30	82.52	12.85	4.64

Table 2. XPS analysis of undoped DLC and Si–DLC films: silicon content, $sp^3/(sp^2 + sp^3)$ ratio, and deconvoluted binding energies (BE, eV) and relative peak areas (%) for C 1s, Si 2p, and O 1s core levels.

Parameter	Bond type	BE [eV]	Undoped DLC	Si–DLC 15W	Si–DLC 20W	Si–DLC 30W
Si (at.%)			—	1.55	3.32	4.64
$sp^3/(sp^2 + sp^3)$			0.81	0.83	0.85	0.86
C 1s	C–sp^2	284.00 to 284.12	18.40	15.99	14.02	12.90
	C–sp^3	284.84 to 284.93	76.92	75.77	76.95	78.11
	C–O	286.14 to 286.40	3.78	7.61	7.91	8.03
	C=O	288.00 to 288.06	0.90	0.62	1.12	0.96
	C–Si	283.56 to 283.80	—	0.00	1.17	3.52
Si 2p	Si–C	100.44 to 100.51	—	66.20	60.30	58.70
	Si–O	101.96 to 102.24	—	33.80	39.70	41.30
O 1s	O=C	531.50 to 531.85	92.21	54.10	54.82	48.03
	O–C	532.90 to 533.10	7.79	13.87	10.24	8.20
	O–Si	532.15 to 532.31	—	32.03	34.94	43.77

Note: *Binding energy ranges represent variation across all samples for each bond type. All percentage values represent relative peak areas, normalized to the total area of the corresponding core-level spectrum. The C–Si bond was not detected in undoped DLC (0 W). Si 2p and O–Si data are not applicable (—) for undoped DLC due to absence of silicon.*

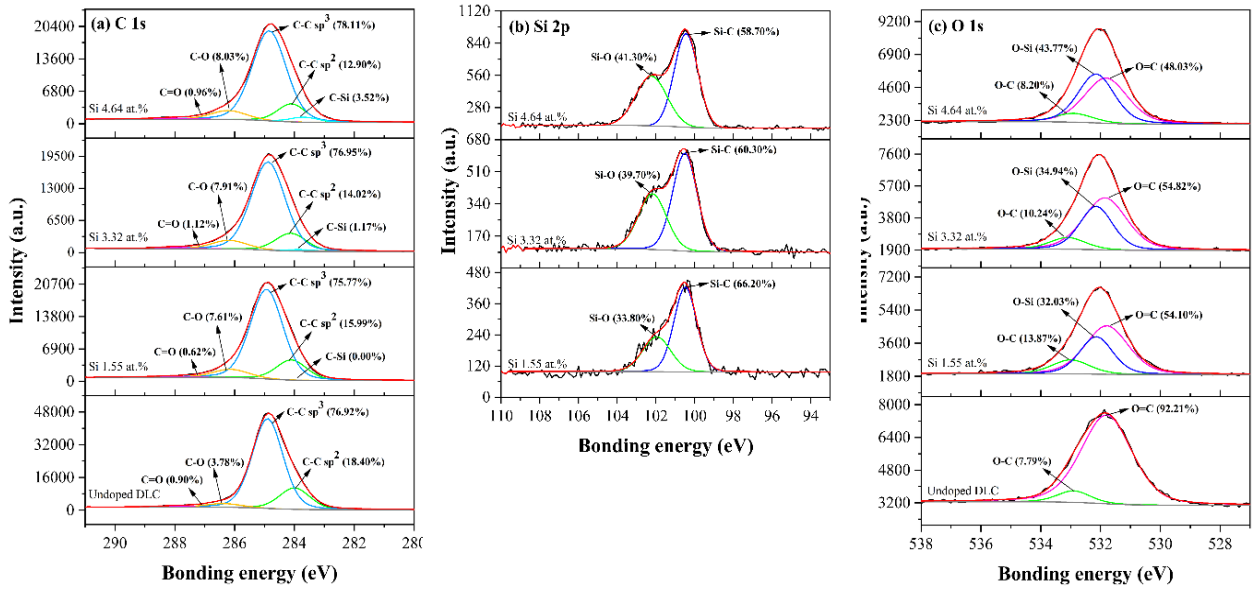

Figure 3. High-resolution XPS spectra of (a) C 1s, (b) Si 2p, and (c) O 1s core levels for undoped DLC and Si–DLC films with varying silicon concentrations. Deconvoluted peaks reveal distinct chemical bonding environments: C–C (sp^2 and sp^3), C–O, C=O, and C–Si bonds in the C 1s spectra; Si–C and Si–O bonds in the Si 2p spectra; and O=C, O–C, and O–Si bonds in the O 1s spectra. Silicon percentages indicated on each spectrum correspond to XPS-determined atomic concentrations. Note: High-resolution Si 2p analysis was not performed for undoped DLC due to absence of detectable silicon in the survey spectrum (Figure 2).

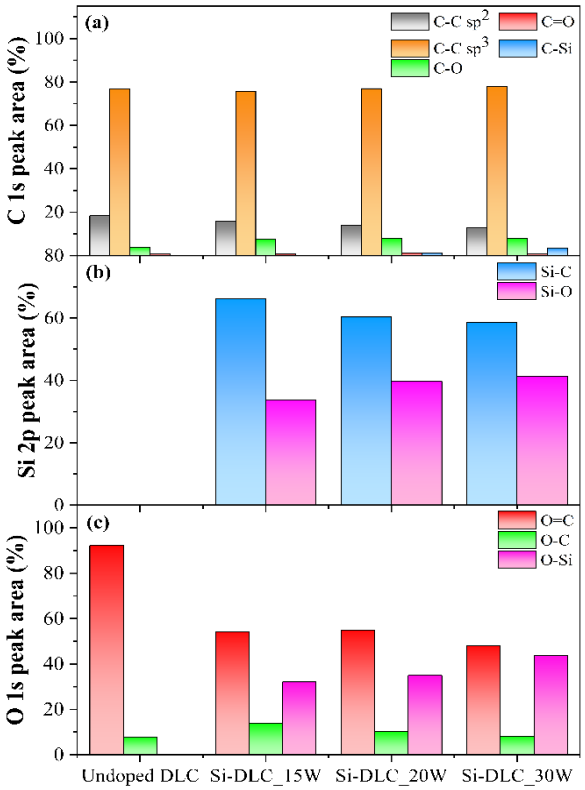

Figure 4. Relative peak areas (%) of chemical bonding states from deconvoluted XPS core-level spectra (a) C 1s, (b) Si 2p, and (c) O 1s for undoped DLC and Si–DLC films with varying silicon concentrations.

The most significant finding involves the increase in sp^3 bonding character upon silicon incorporation. The $sp^3/(sp^2 + sp^3)$ ratio increased progressively from 0.83 in Si–DLC_15W to 0.86 in Si–DLC_30W, as summarized in Table 2. This structural modification indicates that silicon atoms disrupt the graphitic sp^2 network and promote sp^3 bond formation. The mechanism involves silicon's inability to participate in π bonding, which forces neighboring carbon atoms to adopt tetrahedral sp^3 configurations [30,31]. Additionally, the stress relaxation induced by silicon incorporation facilitates the transition from strained sp^2 clusters to more stable sp^3 arrangements [29]. The C–Si contribution increased from 0% in undoped DLC to 3.52% in Si–DLC_30W, directly correlating with silicon content. This trend demonstrates successful chemical incorporation rather than simple physical mixing of silicon and carbon phases.

The O 1s spectra were fitted with three components at 531.74 ± 0.16 eV (O=C), 532.19 ± 0.08 eV (O–Si), and 533.00 ± 0.08 eV (O–C), as shown in Figure 3(c). The proportion of O–Si bonds increased with silicon content, rising from 32.03% in Si–DLC_15W to 43.77% in Si–DLC_30W (Figure 4(c) and Table 2). This trend directly supports the silicon chemical state analysis, which demonstrated increased Si–O bond formation at higher silicon concentrations. The complementary behavior between O–Si and O=C bonding states validates the competitive oxygen incorporation mechanism. As the O–Si bond content increased from 32.03% to 43.77%, both O=C and O–C bond contents decreased. The O=C bonds declined from 54.10% to 48.03%, while O–C bonds dropped from 13.87% to 8.20%. This distribution suggests that oxygen preferentially bonds with silicon rather than carbon, consistent with the well-known higher oxygen affinity of silicon.

3.2 Raman spectroscopy analysis

Raman spectroscopy provided detailed insights into the microstructural changes induced by the incorporation of silicon into DLC films. Figure 5(a) presents the Raman spectra for undoped DLC and Si–DLC films across the 1180 cm^{-1} to 1800 cm^{-1} range. All spectra exhibit two prominent features. The D peak, centered at approximately 1373.60 cm^{-1}, corresponds to disordered sp^2-bonded carbon. The G peak centered around 1550.30 cm^{-1} relates to sp^2 bond stretching in

graphitic configurations. Gaussian fitting analysis extracted precise peak positions, full width at half maximum (FWHM) values, and intensity ratios, as summarized in Table 3.

Silicon incorporation induces modifications to the carbon bonding network, as indicated by two spectroscopic parameters. Figure 5(b) confirms a shift of the G peak position toward lower wavenumbers with increasing silicon content. The G peak shifts from 1558.11 ± 7.40 cm^{-1} in undoped DLC to 1542.64 ± 4.40 cm^{-1} for Si–DLC_30W (4.64 at.% Si). The I_D/I_G ratio also shows a decreasing trend with increasing silicon content, from 0.41 ± 0.08 in undoped DLC to 0.39 ± 0.08, 0.29 ± 0.04, and 0.24 ± 0.04 for the respective Si–DLC samples.

The Ferrari–Robertson model for amorphous carbons provides the theoretical framework for interpreting these observations [32]. A reduction in sp^2 cluster size drives the G band to lower wavenumbers. The corresponding decrease in I_D/I_G accompanies the structural transition. Both metrics serve as established qualitative indicators of reduced sp^2 clustering and enhanced tetrahedral structure. This interpretation aligns with our XPS-derived increase in $sp^3/(sp^2 + sp^3)$ ratios and the detected C–Si bonding upon Si addition (Table 2). Silicon atoms disrupt π-conjugated sp^2 domains and promote tetrahedral configurations within the DLC matrix.

Wang *et al.* [33] demonstrated that increasing the Si content reduces the I_D/I_G ratio and shifts the G band to lower wavenumbers. Their study linked these spectral changes to diminished sp^2 domain sizes and improved thermal stability. Wan *et al.* [34] observed similar decreases in I_D/I_G upon Si incorporation, which correlated with higher effective sp^3/sp^2 ratios. The comprehensive review by Meškinis *et al.* [29] emphasized Si-induced formation of Si–C and Si–Ox bonds, accompanied by stress reduction and Raman signatures characteristic of increased tetrahedral bonding. These previous reports validate our microstructural and spectroscopic observations.

3.3 Optical property modifications

Spectroscopic ellipsometry (SE) enabled analysis of optical constants in the DLC films. Refractive index (n) and extinction coefficient (k) were determined over the wavelength range of 245 nm to 1000 nm, as shown in Figure 6.

Both optical parameters exhibited decreases with increasing silicon incorporation. The extinction coefficient declined relative to the undoped DLC baseline across all measured wavelengths, with the most pronounced reductions at wavelengths below 500 nm.

Figure 7 quantifies these optical modifications through wavelength-averaged values. The wavelength-averaged refractive index decreased linearly from 2.64 to 2.60 with increasing silicon content, while the wavelength-averaged extinction coefficient decreased slightly from 1.05 to 0.97. These changes in optical properties correlate directly with the microstructural modifications revealed by XPS and Raman spectroscopy.

The observed optical behavior is a result of fundamental modifications in the carbon bonding network upon silicon incorporation. XPS analysis confirmed an increased $sp^3/(sp^2 + sp^3)$ ratio, alongside the formation of C–Si bonds, reaching 3.52% in the highest-doped films. This enhanced tetrahedral structure reduces the density of sp^2 domains responsible for optical absorption in the visible region [3,35]. Raman spectroscopy provided complementary evidence through systematic G-peak shifts to lower wavenumbers and decreased I_D/I_G ratios, which indicate reduced graphitic clustering and strengthened diamond-like bonding networks [32].

The correlation between optical constants and carbon hybridization states follows established relationships for amorphous carbon materials. Earlier studies demonstrated that the refractive index and extinction coefficient are inversely dependent on the sp^3/sp^2 ratio in DLC films [23,29]. Silicon atoms disrupt π-bonding networks by forcing neighboring carbon atoms into tetrahedral configurations, thereby reducing the electronic states responsible for optical absorption [33,36]. This mechanism explains the concurrent improvements in optical transparency and structural ordering observed in our Si-DLC films.

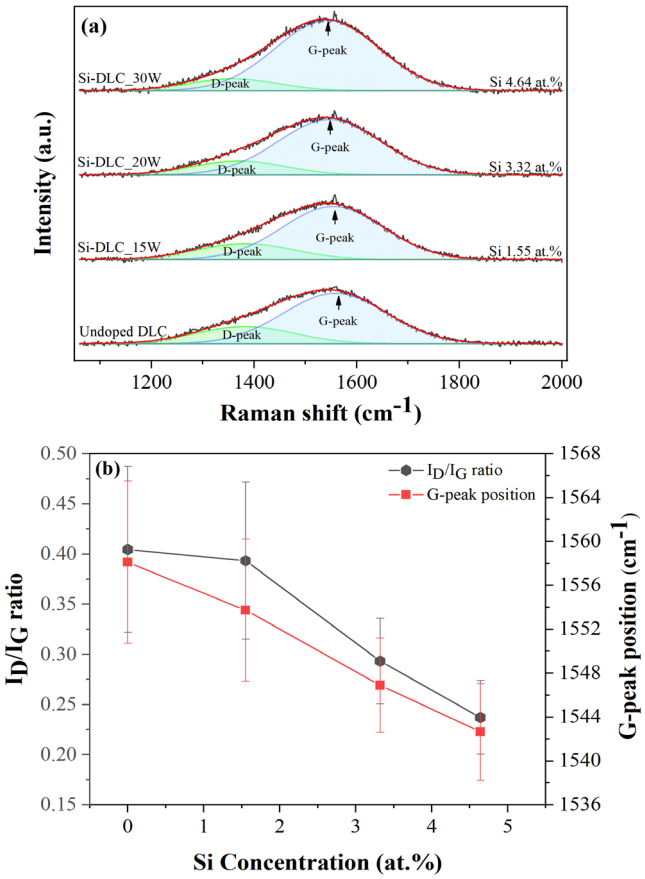

Figure 5. (a) Raman spectra of DLC films with varying silicon contents, and (b) the corresponding I_D/I_G intensity ratio and G peak position of both undoped DLC and Si–DLC films as a function of silicon concentration.

Table 3. Summary of Raman fitting parameters for DLC and Si–DLC films.

Sample	D-peak [cm^{-1}]	G-peak [cm^{-1}]	FWHM (D)	FWHM (G)	I_D/I_G
undoped DLC	1382.19	1558.11	214.78	231.52	0.41
Si–DLC_15W	1383.35	1553.74	222.09	231.16	0.39
Si–DLC_20W	1370.10	1546.90	211.67	235.99	0.29
Si–DLC_30W	1358.95	1542.64	203.76	237.70	0.24

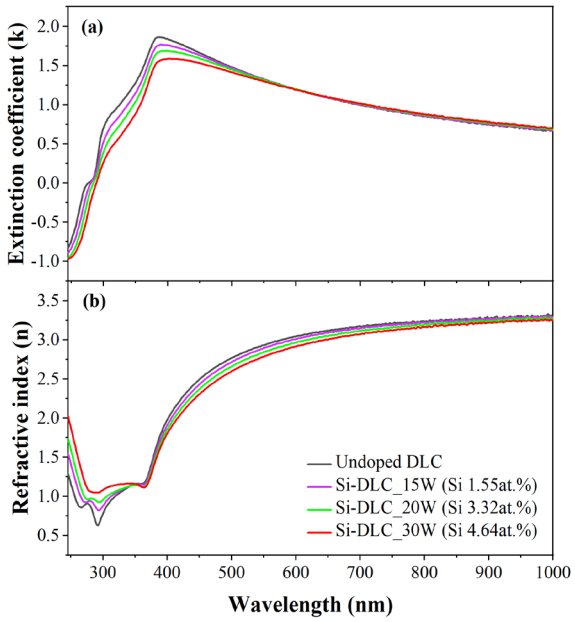

Figure 6. (a) Extinction coefficient, and (b) refractive index as functions of wavelength for undoped DLC and Si–DLC films with different silicon contents.

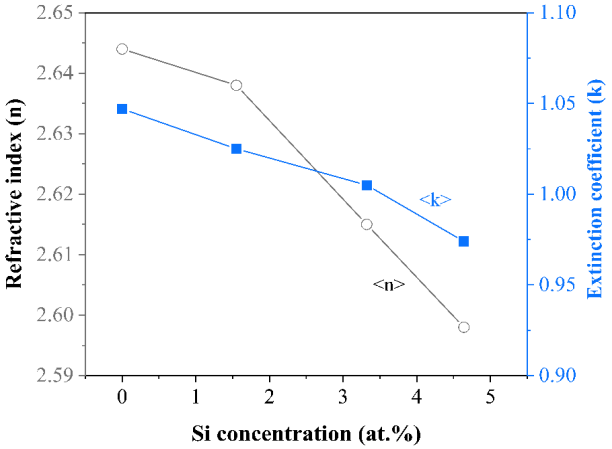

Figure 7. Variation of the wavelength-averaged refractive index ⟨n⟩ and extinction coefficient ⟨k⟩ as a function of XPS-measured silicon concentration for undoped DLC and Si–DLC films.

3.4 Non-destructive silicon quantification via ellipsometry

Spectroscopic ellipsometry (SE) determines optical properties of thin films through measurement of polarization state changes upon light reflection or transmission. This technique quantifies two fundamental parameters, namely, the amplitude ratio (Ψ) and the phase difference (Δ), both of which are highly sensitive to film composition, thickness, and optical properties [23]. While SE provides rapid, non-destructive characterization, extracting compositional information from doped films requires appropriate optical modeling to relate measured parameters to dopant concentration. For silicon content estimation in Si–DLC films, we implemented an optical model based on the Bruggeman effective medium approximation (EMA), a well-established theoretical framework for describing materials composed of multiple distinct phases [36,37]. The Bruggeman EMA treats composite materials as homogeneous effective media with optical properties determined by the volume fractions and dielectric functions of constituent phases [38]. This approach proves particularly suitable for Si–DLC films at the investigated doping levels, where silicon incorporation modifies the optical response of the carbon matrix in a predictable manner.

The Bruggeman formulation calculates the effective complex dielectric function (ε_{eff}) of a two-component mixture according to

$$f_{Si}\frac{\varepsilon_{Si}-\varepsilon_{eff}}{\varepsilon_{Si}+2\varepsilon_{eff}}+(1-f_{Si})\frac{\varepsilon_{DLC}-\varepsilon_{eff}}{\varepsilon_{DLC}+2\varepsilon_{eff}}=0 \quad (1)$$

where f_{Si} represents the silicon volume fraction, ε_{Si} and ε_{DLC} are the complex dielectric functions of amorphous silicon and DLC respectively, and ε_{eff} is the effective medium dielectric function [37]. The depolarization factor inherent in this formulation equals 1/3, corresponding to spherically symmetric inclusions randomly dispersed within the effective medium [38]. This assumption is appropriate when both components are intermixed at the nanoscale without preferential orientation.

Reference optical constants for the EMA components were obtained from two sources. The DLC component was represented by optical constants measured from the undoped DLC film (0 W RF power) through spectroscopic ellipsometry, which contained 92.66 at.% C and 7.34 at.% O according to XPS analysis. The amorphous silicon component was characterized using optical constants from the CompleteEASE software database (J.A. Woollam Co., Inc.).

Silicon volume fractions were determined through iterative regression analysis using CompleteEASE software. The fitting algorithm solves the Bruggeman equation for ε_{eff} at each wavelength in the measured spectral range (245 nm to 1000 nm), then calculates the Fresnel reflection coefficients for the multilayer structure (ambient/film/substrate) and generates model Ψ and Δ values. The minimization algorithm in the software adjusts the silicon volume fraction f_{Si} and film thickness to minimize the mean squared error (MSE) between experimental and calculated ellipsometric spectra.

Figure 8 presents the experimental and Bruggeman EMA-modeled ellipsometric parameters as functions of wavelength for undoped DLC and Si–DLC films with varying RF power corresponding to different silicon content. The excellent agreement between experimental data and model calculations across the entire spectral range validates the two-component effective medium representation. The mean squared error for the Bruggeman EMA fits ranged from 6.6 to 9.3 across all samples (average of 7.6 ± 1.2), indicating high-quality agreement between the model and experimental ellipsometric spectra. Table 4 summarizes the ellipsometric fitting results, including silicon volume fractions derived from the Bruggeman EMA model and corresponding film thicknesses.

The correlation between ellipsometry-derived silicon content and XPS measurements demonstrates the quantitative accuracy of the EMA approach. Figure 9 reveals a strong linear relationship between silicon volume percentages from EMA modeling and atomic percentages from XPS analysis. Weighted linear regression, with each point weighted by the inverse square of its uncertainty in Table 4, yields the equation of $y = (0.82 \pm 0.10)x + (0.05 \pm 0.10)$ with an exceptional correlation coefficient $R^2 = 0.97$, where x represents XPS-measured silicon atomic percent and y represents EMA-derived silicon volume percent. The near-zero intercept (0.05 ± 0.10) indicates negligible systematic offset at low concentrations, while the regression passes through the origin within experimental uncertainty.

Table 4. Silicon volume fractions and film thicknesses determined by spectroscopic ellipsometry with Bruggeman EMA modeling.

Sample	RF power [W]	Si volume fraction [vol%]	Film thickness [nm]	MSE
undoped DLC	0	0.03 ± 0.06	21.5 ± 0.2	6.6
Si–DLC_15W	15	1.90 ± 0.26	20.7 ± 0.7	6.8
Si–DLC_20W	20	2.47 ± 0.29	21.6 ± 0.7	7.7
Si–DLC_30W	30	3.77 ± 0.38	22.7 ± 0.8	9.3

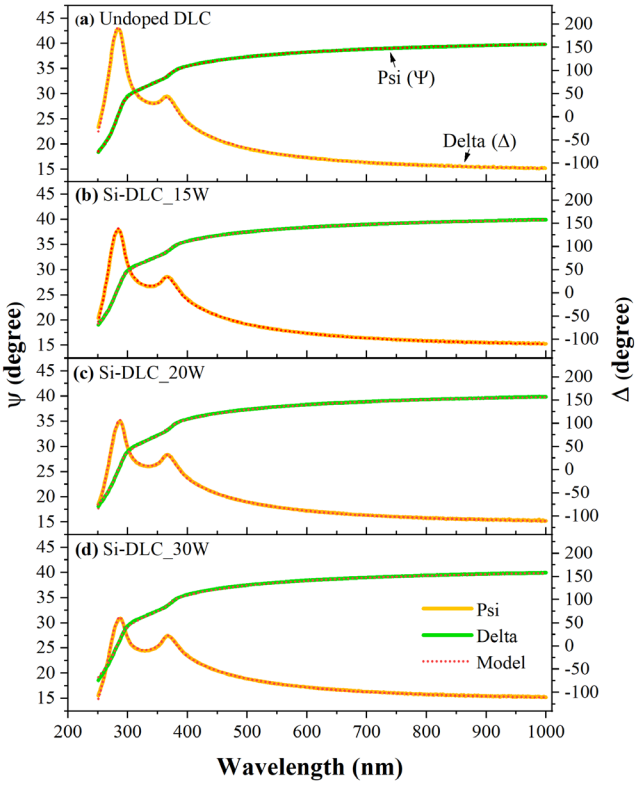

Figure 8. Experimental and modeled values of Psi and Delta obtained by spectroscopic ellipsometry (SE) as a function of wavelength (a) undoped DLC and Si–DLC at RF powers of (b) 15 W, (c) 20 W, and (d) 30 W.

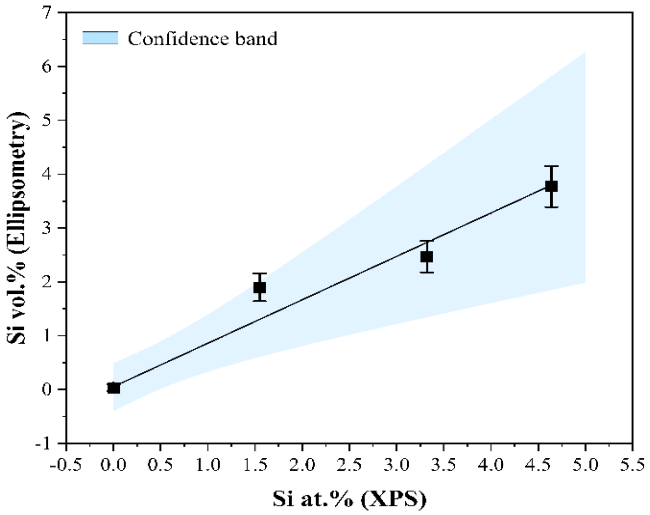

Figure 9. Correlation between Si content obtained from XPS analysis and Si volume fraction estimated using the Bruggeman EMA model from spectroscopic ellipsometry data. The solid black line shows the weighted linear regression fit. The shaded region represents the 95% confidence band. Error bars represent one standard deviation from repeated ellipsometric measurements (y-axis, Table 4).

To assess the statistical robustness of the calibration, a 95% confidence band was constructed around the weighted linear regression line. The band quantifies the uncertainty in the fitted calibration line and is narrowest at low silicon content, where the calibration data carry the greatest statistical weight. Its width mainly reflects the small calibration set (n = 4); additional calibration points in future work would narrow the band and further improve the precision of this non-destructive approach.

3.5 Discussion

The regression slope of 0.82 ± 0.10, slightly below unity, indicates systematic underestimation of silicon content by the EMA model relative to XPS measurements. This deviation arises from fundamental differences between the characterization techniques and simplifications in the optical model. Several factors contribute to this offset as discussed below.

The Bruggeman model rests on three simplifications. First, its fixed depolarization factor of 1/3 assumes spherical inclusions [38], whereas the Si–C and Si–O clusters in the amorphous network are likely irregular, which biases the derived volume fractions increasingly as the silicon content grows. Second, the film is treated as homogeneous, although the rising total oxygen content (Table 1) and the tendency of silicon to oxidize near the surface suggest possible depth gradients; because ellipsometry averages over the full ~21 nm thickness while XPS probes only the top 5 nm to 10 nm, such gradients would also contribute to the sub-unity slope. Third, representing all silicon by a-Si optical constants ignores the Si–O fraction (33.8% to 41.3%, Table 2), which likely accounts for much of the slope of 0.82 ± 0.10. Below 5 at.%, these simplifications are acceptable ($R^2 = 0.97$, Table 4), but at higher doping the growing Si–O fraction would progressively degrade the EMA–XPS linearity, so extrapolation beyond the calibrated range should be treated with caution.

Previous EMA applications to doped carbon films have focused on different concentration regimes or dopant species, which helps contextualize our findings. Yaremchuk et al. employed renormalized Maxwell-Garnett EMA for silver quantification at higher concentrations (8 at.% to 22 at.%) in Ag–DLC nanocomposites [24]. At those levels, plasmonic effects from metallic nanoparticles dominate the optical response, requiring a formulation that treats metallic inclusions in a dielectric host. In contrast, our work extends EMA-based composition determination to the low silicon regime (1.55 at.% to 4.64 at.%), where the challenge lies in detecting subtle optical changes against the dominant DLC matrix rather than distinct plasmonic resonances. The strong linear correlation we observe at these lower concentrations demonstrates that Bruggeman EMA remains effective even when dopant-induced optical changes are small.

Li *et al.* applied SE with Bruggeman EMA to extract sp^3/sp^2 ratios in undoped DLC films [23], demonstrating that effective medium

modeling can probe structural information. However, their focus on hybridization state rather than dopant quantification represents a different application. Zimmer *et al.* used SE with Bruggeman EMA to infer boron doping effects in nanocrystalline diamond by analyzing free carrier absorption [25]. The crystalline host material and electronic doping mechanism differ substantially from silicon incorporation in amorphous DLC, where optical modifications arise primarily from structural changes (sp^3 enhancement, reduced graphitic clustering) rather than free carrier effects.

Our approach achieves dopant quantification through direct correlation with XPS, providing a calibrated relationship between optical modeling and atomic composition. The observed slope of 0.82 reflects the simplified two-phase treatment, where actual Si–C and Si–O bonding environments are approximated as pure a-Si inclusions. Despite this simplification, the high correlation coefficient supports the utility of this method as a calibrated tool for process monitoring and quality control within the investigated low-Si range, where rapid relative measurements are often more valuable than absolute precision.

4. Conclusion

This study demonstrates the control of silicon incorporation in diamond-like carbon films through RF magnetron sputtering and establishes a reliable non-destructive method for silicon content quantification. Silicon doping levels from 1.55 at.% to 4.64 at.% were achieved by varying RF power.

Comprehensive characterization revealed significant microstructural modifications upon silicon incorporation. XPS analysis showed formation of C–Si bonds, which confirms silicon integration into the carbon network. Raman spectroscopy provided complementary structural evidence through a G-peak shift to lower wavenumbers and a decreased I_D/I_G ratio. These changes indicate increased tetrahedral carbon bonding and diminished graphitic domain size. Spectroscopic ellipsometry measurements revealed optical property changes, with both extinction coefficient and refractive index decreasing upon silicon incorporation. These optical modifications directly correlate with the structural reorganization observed across all characterization techniques.

The primary contribution involves establishing a non-destructive silicon quantification method using spectroscopic ellipsometry with the Bruggeman effective medium approximation model. Strong linear correlation ($R^2 = 0.97$) between EMA-derived silicon volume percentages and XPS atomic percentages validates this optical approach. The model underestimates silicon content by 18% (slope = 0.82). However, this deviation can be corrected through established calibration protocols.

This non-destructive method offers substantial advantages for industrial applications. The technique enables rapid compositional analysis suitable for in-line quality control during large-scale film production. Real-time silicon content monitoring becomes possible for precise process control. These capabilities address critical manufacturing needs and establish a foundation for optimizing Si-DLC film properties through controlled silicon incorporation.

Acknowledgments

This research was supported by the Industry/University Cooperative project, which provided the facilities and resources essential for conducting this study. The authors would like to give special thanks to Dr. Phuwanai Bunnak, Mongkhol Suwanno and all technicians involved for their valuable suggestions and technical support.

References

[1] A. Grill, “Diamond-like carbon: state of the art,” *Diamond and Related Materials*, vol. 8, no. 2–5, pp. 428–434, 1999.

[2] B. Schultrich, "Tetrahedrally bonded amorphous carbon films I: Basics, structure and preparation," *Springer Series in Materials Science*, vol. 263. Berlin, Heidelberg: Springer, 2018.

[3] J. Robertson, “Diamond-like amorphous carbon,” *Materials Science and Engineering: R: Reports*, vol. 37, no. 4–6, pp. 129–281, 2002.

[4] Q. Wei, R. J. Narayan, A. K. Sharma, J. Sankar, and J. Narayan, “Preparation and mechanical properties of composite diamond-like carbon thin films,” *Journal of Vacuum Science & Technology A*, vol. 17, no. 6, pp. 3406–3414, 1999.

[5] M. Azzi, P. Amirault, M. Paquette, J. E. Klemberg-Sapieha, and L. Martinu, “Corrosion performance and mechanical stability of 316L/DLC coating system: Role of interlayers,” *Surface and Coatings Technology*, vol. 204, no. 24, pp. 3986–3994, 2010.

[6] X. Sui, J. Liu, S. Zhang, J. Yang, and J. Hao, “Microstructure, mechanical and tribological characterization of CrN/DLC/Cr-DLC multilayer coating with improved adhesive wear resistance,” *Applied Surface Science*, vol. 439, pp. 24–32, 2018.

[7] Q. Zeng, and Z. Ning, “High-temperature tribological properties of diamond-like carbon films: A review,” *Reviews on Advanced Materials Science*, vol. 60, no. 1, pp. 276–292, 2021.

[8] H. Sun, L. Yang, H. Wu, and L. Zhao, “Effects of element doping on the structure and properties of diamond-like carbon films: A review,” *Lubricants*, vol. 11, no. 4, p. 186, 2023.

[9] J. Peng, M. Yang, J. Zeng, D. Su, J. Liao, and M. Yick, “Influence of nitrogen doping on the thermal stability of hydrogenated amorphous diamond coating,” *Thin Solid Films*, vol. 709, p. 138188, 2020.

[10] N. Konkhunthot, C. Euaruksakul, P. Photongkam, and P. Wongpanya, “Characterization of diamond-like carbon (DLC) films deposited by filtered cathodic vacuum arc technique,” *Journal of Metals, Materials and Minerals*, vol. 23, no. 1, pp. 35–40, 2013.

[11] P. Ratchayotee, A. Chingsungnoen, and P. Poolcharuansin, “Controlling titanium incorporation in hydrogenated amorphous carbon films via closed-loop feedback in reactive high power impulse magnetron sputtering,” *Journal of Metals, Materials and Minerals*, vol. 34, no. 4, p. 2114, 2024.

[12] Y.-J. Jang, J.-I. Kim, W.-S. Kim, D. H. Kim, and J. Kim, “Thermal stability of Si/SiC/ta-C composite coatings and improvement of tribological properties through high-temperature annealing,” *Scientific Reports*, vol. 12, no. 1, p. 3536, 2022.

[13] M. Rouhani, J. Hobley, F. Chau-Nan Hong, and Y.-R. Jeng, “In-situ thermal stability analysis of amorphous Si-doped carbon films,” *Carbon*, vol. 184, pp. 772–785, 2021.

[14] X. Wang, X. Zhang, C. Wang, Y. Lu, and J. Hao, “High temperature tribology behavior of silicon and nitrogen doped hydrogenated diamond-like carbon (DLC) coatings,” *Tribology International*,

vol. 175, p. 107845, 2022.

[15] S. M. Fayed, D. Chen, S. Li, Y. Zhou, H. Wang, and M. M. Sadawy, "Corrosion behavior and passive stability of multilayer DLC-Si coatings," *Surface and Coatings Technology*, vol. 431, p. 128001, 2022.

[16] D. Bociaga, A. Sobczyk-Guzenda, P. Komorowski, J. Balcerzak, K. Jastrzębski, K. Przybyszewska, and A. Kaczmarek, "Surface characteristics and biological evaluation of Si-DLC coatings fabricated using magnetron sputtering method on Ti_6Al_7Nb substrate," *Nanomaterials*, vol. 9, no. 6, p. 812, 2019.

[17] Z. Yu, J. Shang, Q. Wang, H. Zheng, H. Mei, D. Zhao, X. Liu, J. Ding, and J. Zheng, "Influence of Si content on the microstructure and properties of hydrogenated amorphous carbon films deposited by magnetron sputtering technique," *Coatings*, vol. 15, no. 7, p. 793, 2025.

[18] H. Nakazawa, R. Kamata, and S. Okuno, "Deposition of silicon-doped diamond-like carbon films by plasma-enhanced chemical vapor deposition using an intermittent supply of organosilane," *Diamond and Related Materials*, vol. 51, pp. 7–13, 2015.

[19] T. F. Zhang, Z. X. Wan, J. C. Ding, S. Zhang, Q. M. Wang, and K. H. Kim, "Microstructure and high-temperature tribological properties of Si-doped hydrogenated diamond-like carbon films," *Applied Surface Science*, vol. 435, pp. 963–973, 2018.

[20] G. G. Politano, and C. Versace, "Spectroscopic ellipsometry: Advancements, applications and future prospects in optical characterization," *Spectroscopy Journal*, vol. 1, no. 3, pp. 163–181, 2023.

[21] M. T. Othman, J. A. Lubguban, A. A. Lubguban, S. Gangopadhyay, R. D. Miller, W. Volksen, and H.-C. Kim, "Characterization of porous low-k films using variable angle spectroscopic ellipsometry," *Journal of Applied Physics*, vol. 99, no. 8, p. 083503, 2006.

[22] Y. Liu, J. Qiu, and L. Liu, "Applicability of the effective medium approximation in the ellipsometry of randomly micro-rough solid surfaces," *Optics Express*, vol. 26, no. 13, pp. 16560–16571, 2018.

[23] W. J. Li, Z. R. Song, Y. H. Yu, X. Wang, S. C. Zou, and D. S. Shen, "sp^3/sp^2 ratio in amorphous-carbon thin film by spectroscopic ellipsometry," *Journal of Applied Physics*, vol. 94, no. 1, pp. 284–287, 2003.

[24] I. Yaremchuk, Š. Meškinis, V. Fitio, Y. Bobitski, K. Šlapikas, A. Čiegis, Z. Balevičius, A. Selskis, and S. Tamulevičius, "Spectro-ellipsometric characterization and modeling of plasmonic diamond-like carbon nanocomposite films with embedded Ag nanoparticles," *Nanoscale Research Letters*, vol. 10, no. 1, p. 157, 2015.

[25] A. Zimmer, O. A. Williams, K. Haenen, and H. Terryn, "Optical properties of heavily boron-doped nanocrystalline diamond films studied by spectroscopic ellipsometry," *Applied Physics Letters*, vol. 93, no. 13, p. 131910, 2008.

[26] A. G. Shard, "Practical guides for x-ray photoelectron spectroscopy: Quantitative XPS," *Journal of Vaccuum Science & Technology A*, vol. 38, no. 4, p. 041201, 2020.

[27] G. Greczynski, and L. Hultman, "A step-by-step guide to perform x-ray photoelectron spectroscopy," *Journal of Applied Physics*, vol. 132, no. 1, p. 011101, 2022.

[28] J. Choi, M. Kawaguchi, T. Kato, and M. Ikeyama, "Deposition of Si–DLC film and its microstructural, tribological and corrosion properties," *Microsystem Technologies*, vol. 13, no. 8–10, pp. 1353–1358, 2007.

[29] Š. Meškinis, A. Vasiliauskas, M. Andrulevičius, D. Peckus, S. Tamulevičius, and K. Viskontas, "Diamond like carbon films containing Si: Structure and nonlinear optical properties," *Materials*, vol. 13, no. 4, p. 1003, 2020.

[30] P. R. Riley, P. Joshi, N. Khosla, R. J. Narayan, and J. Narayan, "Formation of Q-carbon with wafer scale integration," *Carbon*, vol. 196, pp. 972–978, 2022.

[31] P. R. Riley, P. Joshi, S. Azizi Machekposhti, R. Sachan, J. Narayan, and R. J. Narayan, "Enhanced vapor transmission barrier properties via silicon-incorporated diamond-like carbon coating," *Polymers*, vol. 13, no. 20, p. 3543, 2021.

[32] A. C. Ferrari, and J. Robertson, "Interpretation of Raman spectra of disordered and amorphous carbon," *Physical Review B*, vol. 61, no. 20, pp. 14095–14107, 2000.

[33] J. Wang, J. Pu, G. Zhang, and L. Wang, "Tailoring the structure and property of silicon-doped diamond-like carbon films by controlling the silicon content," *Surface and Coatings Technology*, vol. 235, pp. 326–332, 2013.

[34] G. J. Wan, P. Yang, R. K. Y. Fu, Y. F. Mei, T. Qiu, S. C. H. Kwok, J. P. Y. Ho, N. Huang, X. L. Wu, and P. K. Chu, "Characteristics and surface energy of silicon-doped diamond-like carbon films fabricated by plasma immersion ion implantation and deposition," *Diamond and Related Materials*, vol. 15, no. 9, pp. 1276–1281, 2006.

[35] Y. Lu, S. Wang, G. Huang, L. Xi, G. Qin, M. Zhu, and H. Chu, "Fabrication and applications of the optical diamond-like carbon films: a review," *Journal of Materials Science*, vol. 57, no. 6, pp. 3971–3992, 2022.

[36] D. P. Dowling, K. Donnelly, M. Monclus, and M. McGuinness, "The use of refractive index as a measure of diamond-like carbon film quality," *Diamond and Related Materials*, vol. 7, no. 2–5, pp. 432–434, 1998.

[37] H. G. Tompkins, "Optical components and the simple PCSA (polarizer, compensator, sample, analyzer) ellipsometer," in Handbook of Ellipsometry, H. G. Tompkins and E. A. Irene, Eds. Norwich, NY: William Andrew Publishing, 2005, pp. 299-328.

[38] D. E. Aspnes, J. B. Theeten, and F. Hottier, "Investigation of effective-medium models of microscopic surface roughness by spectroscopic ellipsometry," *Physical Review B*, vol. 20, no. 8, pp. 3292–3302, 1979.